Authors
Toulson, Benjamin W
Kapnas, Kara M
Fishman, Dmitry A
et al.

Peer reviewed

Competing Pathways in the Near-UV Photochemistry of Acetaldehyde

Benjamin W. Toulson, Kara M. Kapnas, Dmitry A. Fishman and Craig Murray[1]

Department of Chemistry, University of California, Irvine, Irvine CA 92697, USA

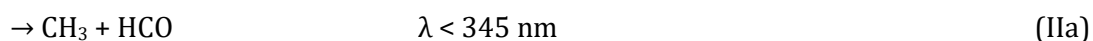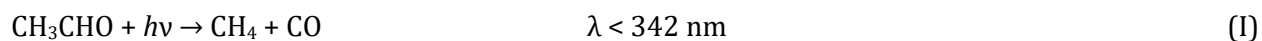[1] Email: craig.murray@uci.edu; Telephone: +1-949-824-4218
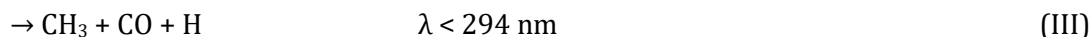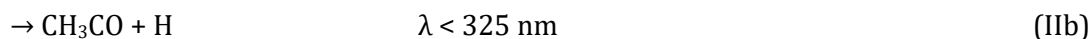
Abstract

Time-resolved ion imaging measurements have been performed to explore the photochemistry of acetaldehyde at photolysis wavelengths spanning the range 265–328 nm. Ion images recorded probing CH_3 radicals with single-photon VUV ionization show different dissociation dynamics in three distinct wavelength regions. At the longest photolysis wavelengths, $\lambda > 318$ nm, CH_3 radicals are formed over tens of nanoseconds with a speed distribution that is consistent with statistical unimolecular dissociation on the S_0 surface following internal conversion. In the range 292 nm $\leq \lambda \leq$ 318 nm, dissociation occurs almost exclusively on the T_1 surface following intersystem crossing and passage over a barrier, leading to the available energy being partitioned primarily into photofragment recoil. The CH_3 speed distributions become bimodal at $\lambda < 292$ nm, in addition to the translationally fast T_1 products a new translationally slow, but non-statistical, component appears and grows in importance as the photolysis wavelength is decreased. Photofragment excitation (PHOFEX) spectra of CH_3CHO obtained probing CH_3 and HCO products are identical across the absorption band, indicating that three-body fragmentation is not responsible for the non-statistical slow component. Rather, translationally slow products are attributed to dissociation on S_0, accessed via a conical intersection between the S_1 and S_0 surfaces at extended C–C distances. Time-resolved ion images of CH_3 radicals measured using a picosecond laser operating at a photolysis wavelength of 266 nm show that product formation on T_1 and S_0 via the conical intersection occurs with time constants of 240 and 560 ps, respectively.

2

Introduction

Interest in the photochemistry of acetaldehyde is driven by its importance in atmospheric chemistry, where absorption of sunlight induces decomposition to form reactive radical species. From a fundamental perspective, as a small molecule amenable to rigorous experimental and theoretical investigation, acetaldehyde presents particularly rich photochemistry and photophysics. The near-UV absorption spectrum of acetaldehyde is a broad continuum spanning 240–336 nm, with diffuse vibrational structure superimposed.[1] The first absorption band arises from excitation of an electron from the oxygen lone pair to the lowest π^* orbital localized on the C–O bond. The 0_0^0 origin band of the $S_1 \leftarrow S_0$ electronic transition has been identified at 335.9 nm (29771 cm^{-1}) by laser-induced fluorescence measurements.[2] The spectra show that the hydrogen-wagging and methyl-torsion modes are active, consistent with a large geometric rearrangement at the S_1 minimum.[2-6] The spectroscopy of the triplet state has been explored using laser-induced phosphorescence, with the 0_0^0 origin band of the $T_1 \leftarrow S_0$ electronic transition identified at 367.1 nm (27241 cm^{-1}).[7] At all wavelengths, there is competition between radiative and non-radiative decay processes. Both fluorescence and phosphorescence quantum yields decline steeply at $\lambda < 319$ nm due to the onset of Norrish Type I dissociation over a barrier on the T_1 surface to form $CH_3 + HCO$.[6,8,9] Quantum beats have been observed in the fluorescence at longer wavelengths, indicating reversible population transfer between the S_1 and T_1 states.[8-10]

At least four chemically distinct product channels are energetically accessible following excitation in the near UV, and each can be reached by multiple photodissociation pathways, giving acetaldehyde a particularly rich photochemistry. The major dissociation products and their threshold wavelengths are

$$CH_3CHO + h\nu \rightarrow CH_4 + CO \qquad\qquad \lambda < 342 \text{ nm} \qquad\qquad\qquad (I)$$

$$\rightarrow CH_3 + HCO \qquad\qquad \lambda < 345 \text{ nm} \qquad\qquad\qquad (IIa)$$

$$\rightarrow CH_3CO + H \qquad\qquad \lambda < 325 \text{ nm} \qquad\qquad\qquad (IIb)$$

$$\rightarrow CH_3 + CO + H \qquad\qquad \lambda < 294 \text{ nm} \qquad\qquad\qquad (III)$$

Threshold wavelengths are calculated from 0 K thermodynamic data obtained from the Argonne National Lab Active Thermochemical Tables (ATcT).[11] The threshold wavelength for channel I product formation reflects the barrier to dissociation on the S_0 surface.
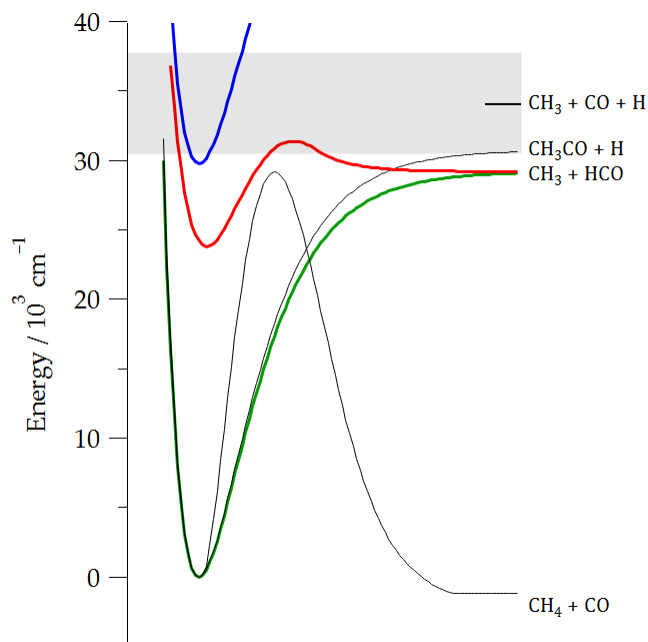

Figure 1 illustrates the key features of the S_0, S_1 and T_1 potential energy surfaces of acetaldehyde.

The molecular products $CH_4 + CO$ (channel I) are formed with significant quantum yield at shorter excitation wavelengths ($\lambda < 292$ nm).[1] Molecular products can be formed by dissociation on the S_0 surface via a conventional tight transition state following internal conversion (IC), or alternatively by roaming. Gherman *et al.* identified CO products exclusively in $v = 0$ following photolysis at 248nm, observing a near-Boltzmann 1300±90 K rotational distribution that was interpreted as being due to dissociation over a barrier on the S_0 surface following internal conversion.[12] Trajectory calculations initiated at the S_0 TS leads to rotationally excited CO products and partitioning of a large fraction of the available energy into translational recoil, in agreement qualitative with the experimental

observations.[13,14]   Acetaldehyde was the second molecule to show evidence of photochemical roaming, with the observation of low-J CO formed in conjunction with highly internally excited CH_4,[15–18] consistent with the dynamical signatures established for roaming in formaldehyde.[19–21] Quasi-classical trajectory calculations on *ab initio* potential surfaces supported this interpretation and indicated that roaming involved frustrated dissociation and subsequent intramolecular reaction between the CH_3 + HCO radical products.[17,22,23] More recent ion imaging experiments, however, have identified translationally slow low-J CO products, with an onset wavelength consistent with the threshold for channel IIb, leading to the suggestion that the radical products CH_3CO + H substantially contribute to roaming.[24]

Of the two radical product channels, IIa is most important and dominates the long wavelength ($\lambda >$ 266 nm) photochemistry.[1]   The radical products CH_3 + HCO can be formed via unimolecular dissociation on S_0 following internal conversion or, if sufficient energy is available, dissociation over a barrier on the T_1 surface following intersystem crossing. Involvement of the T_1 surface was initially proposed and first confirmed experimentally by Horowitz and Calvert.[25,26] Threshold wavelengths for dissociation on T_1 between 318.3–323.0 nm have been estimated using a variety of experimental techniques, including fluorescence lifetime collapse and the onset of product formation.[27–32] Laser-induced fluorescence detection of HCO products following photolysis above the T_1 barrier has been used to identify modest rotational excitation and a tendency for vibrational excitation at shorter wavelengths.[27,28,33,34] The energy disposal has been justified based on *ab initio* calculations of the T_1 transition state geometry and trajectory calculations that explore the dissociation dynamics.[35–38] Time-resolved experiments have characterized the appearance times of HCO products as many tens of nanoseconds following photolysis at wavelengths that excite just above the T_1 barrier and sub-nanosecond at 266 nm.[39–41] Ion imaging experiments probing CH_3 and HCO photoproducts confirm that the available energy is partitioned primarily into translation following excitation above the T_1 barrier, although the degree of internal excitation in the products increases at shorter

wavelengths.[29,31,32,42]   Dissociation on the S_0 surface at longer wavelengths was confirmed by Heazlewood *et al*. who observed distinct HCO product state distributions following photolysis above and below the T_1 barrier.[30]   HCO products are formed on S_0 with an effectively statistical product state distribution, while those formed on T_1 retain dynamical signatures of the barrier. Trajectory calculations incorporating surface hopping involving the S_1, T_1 and S_0 states have explored the branching between CH_3 + HCO products over a broad range of photolysis wavelengths.[38] Experiments performed with partially deuterated CD_3HCO isotopomer identified both HCO and DCO products following excitation to S_1 below the T_1 barrier indicating significant isotope scrambling prior to dissociation on the S_0 surface.[43]   Collisions can stabilize the enol form, vinyl alcohol, and photo-tautomerization may be an efficient route to formation organic acids in the troposphere.[44,45]

At wavelengths shorter than 294 nm, the triple fragmentation channel (III) becomes energetically accessible. Triple fragmentation in acetaldehyde was first postulated by de Wit *et al*. and modelled using a two-step phase space theory calculation that predicts product translational energy distributions similar to those obtained by roaming.[46] Experimental evidence for triple fragmentation at 248 nm comes from time-resolved FTIR emission spectroscopy and also cavity ring-down spectroscopy measurements that indirectly determined radical product yields following conversion to HO_2.[47,48] Curiously, both studies conclude that the radical channel IIa is inactive at 248 nm. This observation is in contrast to earlier estimates,[49] which suggest a quantum yield >10% at this wavelength. Ion imaging measurements have also detecting H atoms directly.[16]

In this paper, we report a study of acetaldehyde photochemistry following excitation at wavelengths between 265–328 nm. Ion imaging experiments using single-photon VUV ionization of CH_3 radicals show three distinct competitive photochemical mechanisms. At the longest wavelengths products are formed via statistical unimolecular dissociation on the S_0 surface. Dissociation on the T_1 surface dominates once energetically accessible, leading to translationally fast products. A translationally slow, but non-statistical, channel that opens at shorter wavelengths is assigned to dissociation on S_0,

accessed via a conical intersection. The relative yields of CH_3 and HCO products are determined from photofragment excitation action spectra, and suggest that triple fragmentation is not a significant dissociation mechanism over the wavelength range studied. Picosecond time-resolved ion imaging measurements at 266 nm show that two competitive mechanisms for product formation are active. Product formation on T_1 is likely limited by the rate of $S_1 \rightarrow T_1$ intersystem crossing, while internal conversion via a long range S_1/S_0 conical intersection leads to S_0 products that form a factor of two more slowly.

Experimental methods

Experiments were performed in a velocity-map ion imaging mass spectrometer that has been described in detail previously.[50] Ion images were recorded using direct-current (DC) slice velocity map imaging.[51] PHOFEX spectra were recorded with the mass spectrometer operating in a conventional Wiley-McLaren time-of-flight arrangement. Ar carrier gas was flowed over a sample of acetaldehyde (Sigma-Aldrich >99.5% purity) in a stainless steel finger that was cooled in an ice bath and expanded into high vacuum from a stagnation pressure of 1 atm using a solenoid pulsed valve (General Valve, Series 9). The expansion of the 30% CH_3HCO/Ar was skimmed (Beam Dynamics) to form a molecular beam before being intersected by counter-propagating photolysis and ionization laser beams. A stack of custom DC slice imaging electrodes accelerated the resultant ions towards a microchannel plate and phosphor screen assembly (Photonis) fitted with a fast, high voltage gate module (Photek GM-MCP-2). The phosphorescence from the screen was monitored by a silicon photomultiplier (SenSL) to obtain conventional time-of-flight mass spectra. For DC slice imaging experiments, a CCD camera (Basler a312f) captured the spatial distribution of mass-selected and sliced ions on the detector. Ion images were acquired while gating the detector to obtain the central ~20 ns of the ion packet. Photolysis and probe laser pulse energies were monitored with a photodiode (Thorlabs DET10a) that had been previously calibrated against an energy meter (Gentec

Maestro). SPM and photodiode signals were digitized by an oscilloscope (LeCroy HDO4054) interfaced to a data acquisition PC running custom written software (National Instruments LabVIEW).

Experiments were performed using lasers with both nanosecond and picosecond pulse durations. In both cases, products were detected using single photon VUV ionization. For the nanosecond experiments, a mid-band Nd:YAG-pumped optical parametric oscillator (OPO) (Continuum Surelite EX and Horizon II) was used to generate photolysis pulses spanning the wavelength range 260–328 nm with a linewidth of 5–7 cm^{-1}. The photolysis beam was loosely focused into the ionization region of the mass spectrometer with an uncoated fused silica lens of focal length f = 1000 mm. The pulse energy varied from 1.1 to 2 mJ across the wavelength range. VUV radiation at 118.2 nm (10.49 eV) was produced by 3rd harmonic generation in Xe/Ar of the frequency-tripled output of a Nd:YAG laser (Continuum Surelite II–10). A static gas cell containing a Xe/Ar mixture (10:1) at a total pressure of ~80 Torr was separated from the ionization chamber by a MgF_2 lens that focused the 118.2 nm into the molecular beam while re-collimating the residual 355 nm.[52] A digital delay generator (Quantum Composers, 9528) was used to control the time delay between the photolysis and ionization pulses.

The picosecond experiments used the 266 nm and 355 nm output from a Nd:YAG laser (Ekspla PL2143), which generated pulses of 28 ps duration at a repletion rate of 10 Hz. The typical pulse energy at 266 nm was 0.5 mJ, while 2.1 mJ of 355 nm was used to generate picosecond duration VUV pulses in the Xe/Ar gas cell as described above. The time delay between the photolysis and ionization pulses was varied over a 2 ns range using a computer-controlled delay line. All other aspects of the experimental apparatus were identical to those used in the experiments performed with the nanosecond laser systems.

Results

The 118.2 nm probe radiation can ionize all polyatomic radical photodissociation products as well as the parent CH_3CHO. The molecular products CH_4 and CO both have ionization energies greater than the 10.49 eV photon energy and were not observed. Two-color signals attributable to ionized CH_3 and HCO photofragments were evident in the time-of-flight mass spectrum, but no signal due to CH_3CO was observed at any photolysis wavelength within the signal to noise. The ionization cross-sections of CH_3 and HCO are similar in magnitude near 118 nm and relatively small ($\sim 5 \times 10^{-18}$ cm^2).[42,53,54] However, ionization is universal. That is, the ionization efficiency is independent of the rovibrational state of the products, which readily compensates for the apparent limitation on the detection sensitivity.[55]

A significant problem for measurements of CH_3CHO photolysis is formation of clusters in the supersonic expansion, as previously noted by Lee *et al.*[24] Peaks corresponding to $(CH_3CHO)_n$ clusters up to $n = 5$ were readily observed in the mass spectrum following VUV ionization. Dissociation of CH_3CHO molecules in clusters produces a translationally slow component that dominates the center of the CH_3 ion images. The cluster contribution could be removed almost completely by careful adjustment of the expansion conditions and operating in the earliest part of the gas pulse. Cluster signals were minimized while monitoring the ion images obtained at a photolysis wavelength of 308 nm. Under cluster-free conditions, the CH_3 ion image is a clean, isotropic ring with a narrow speed distribution centered at 1700 m s^{-1}. Figure 2 shows DC slice ion images of CH_3 photoproducts products at 308 nm, measured under cluster-forming and cluster-free conditions. The expansion conditions were optimized to remove the cluster contribution prior to all measurements.

1. Nanosecond ion imaging

DC sliced velocity-map ion images of CH_3 photoproducts were recorded following excitation of CH_3CHO from 265 nm to 328 nm in 1 nm intervals, spanning available energies E_{AVL} = 1540–8930

cm^{-1} above the dissociation energy for channel IIa ($D_{0,\text{IIa}}$ = 28950 cm^{-1}). Speed and angular distributions were obtained by direct integration of the sliced images over angular and radial coordinates. The angular distributions were universally isotropic, indicating dissociation on a time scale that is long relative to the rotational period of the electronically excited acetaldehyde. The complete set of normalized CH$_3$ speed distributions is shown as an intensity plot in Figure 3. The observed CH$_3$ speed distributions are wavelength-dependent, but can be broadly categorized into the three regions labeled A, B and C.

Region A (λ > 318 nm) corresponds to excitation energies below the T$_1$ barrier of 31400±50 cm^{-1} and consequently products can only be formed on the S$_0$ surface.[31] Few ion counts were recorded at the short photolysis-probe delays (40 ns) used to obtain the data in Figure 3, although translationally slow methyl products are detected at longer delays as described below. A sharp increase in the total ion count is observed at $\lambda \leq$ 318 nm (Region B). Throughout Region B, sufficient energy is available to overcome the T$_1$ barrier, leading to CH$_3$ radicals with recoil speeds that peak near, and extend to, the maximum allowed by energy conservation. As the photolysis wavelength is decreased, the speed distributions broaden and the most probable speeds deviate increasingly from v_{max}. This trend continues through Region C ($\lambda \leq$ 292 nm), whereupon the speed distributions also become bimodal. A new translationally slow component first appears weakly at 292 nm and increases in magnitude as the wavelength is further decreased. We assert here, and justify later, that the slow component at short wavelengths results from channel IIa products formed on the S$_0$ surface.

The methyl radical speed distributions were converted into total translational energy distributions using

$$P(E_\text{T}) \propto P(v)/v$$

where

$$E_T = \frac{1}{2} m_{CH_3} \left(1 + \frac{m_{CH_3}}{m_{HCO}} \right) v_{CH_3}^2$$

and it is implicitly assumed that formyl is the momentum-matched co-fragment. The available energy following dissociation, E_{AVL}, is partitioned between internal (rotational and vibrational) energy of the fragments, E_{INT}, and relative translation, E_T, according to

$$E_{AVL} = h\nu - D_0 = E_{INT} + E_T$$

where $h\nu$ is the photolysis photon energy and D_0 is the channel IIa dissociation energy. Since single-photon VUV ionization of CH_3 is non-state-selective, the values of E_{INT} determined in these measurements are the sums of the internal energies of the CH_3 and HCO fragments. Normalized E_T distributions obtained at six selected photolysis wavelengths spanning Regions B (316 nm, 306 nm, and 296 nm) and Region C (286 nm, 276 nm, and 266 nm) are shown in Figure 4. These wavelengths correspond to excitation energies ranging from 250–6200 cm^{-1} above the T_1 barrier. Excitation just above the T_1 barrier results in a narrow E_T distribution that cuts off sharply on the high-E_T side near the energetic limit. As the photolysis wavelength is decreased through Region B, the E_T distributions broaden and increasingly shift away from the energetic limit, indicating that a greater fraction of the available energy is partitioned into E_{INT}. The onset and subsequent growth of the slow S_0 component through Region C is evident in Figure 4, while the wavelength-dependent evolution of the T_1 component continues with the same trend established in Region B.

The bimodal E_T distributions in Region C were decomposed into relative contributions of the fast T_1 and slow S_0 components by fitting to sums of exponentially-modified Gaussian functions (also shown in Figure 4). The branching between the T_1 and short-wavelength S_0 components is shown in Figure 5. Products formed on S_0 account for ~10–15% of the total near 292 nm and increases to around 40% at the shortest wavelengths used in the measurements. The average translational energy and, by conservation of energy, average radical internal energy are shown as a function of E_{AVL} in Figure

11

6. For products formed on the T_1 surface, both $\langle E_T \rangle$ and $\langle E_{INT} \rangle$ increase approximately linearly with E_{AVL}. $\langle E_T \rangle$ ranges from ~2000 cm^{-1} following excitation at 318 nm, just above the T_1 threshold, to ~5000 cm^{-1} at 265 nm while $\langle E_{INT} \rangle$ correspondingly increases by an order of magnitude from ~400 cm^{-1} to ~4000 cm^{-1}. The fraction of E_{AVL} partitioned into relative translation decreases from 0.85 to 0.56 over the same range. In contrast, products formed on S_0 in Region C have significantly smaller $\langle E_T \rangle$ values that increase only slightly as the available energy increases, ranging from ~700–1240 cm^{-1}. The fraction of available energy partitioned into translation is remarkably consistent across this range at ~0.15. $\langle E_{INT} \rangle$ for products formed on S_0 following excitation almost doubles from ~4000 cm^{-1} near the onset wavelength of 292 nm to 7500 cm^{-1} at 265 nm.

Time-resolved ion images of CH_3 products were recorded at photolysis wavelengths of 317 nm and 320 nm while stepping the photolysis-probe time delay between 30–210 ns to explore the photochemistry following excitation near the T_1 barrier. Excitation at 320 nm prepares acetaldehyde in the S_1 state with an energy 150 cm^{-1} below the T_1 barrier, restricting channel IIa product formation to the S_0 surface. At 317 nm, the excitation energy is 150 cm^{-1} above the barrier and products can form on both the T_1 and S_0 surfaces. The maximum CH_3 speeds allowed by energy conservation following one-photon dissociation at 320 nm and 317 nm are 1550 m s^{-1} and 1650 m s^{-1}, respectively. Figure 7 shows the CH_3 speed distributions measured at delays of 30 ns, 90 ns and 210 ns. The CH_3 speed distributions at both wavelengths can be decomposed into three components; a) a translationally slow feature, that increases in magnitude with increasing delay, b) the narrow fast component due to dissociation on T_1 that peaks near v_{max}, and c) a broad feature extending significantly beyond v_{max}, that decreases in magnitude with increasing delay. While the relative magnitudes of each component are different at each pump wavelength, they each display similar dependences on the photolysis-probe time delay. The time-dependent magnitudes of each component of the CH_3 speed distribution are fit to single exponential loss or growth functions, which are also shown in Figure 7. The time constants are summarized in Table 1.

At 320 nm, the speed distribution is dominated by translationally slow products at long delays. This component grows in with a time constant of 66±9 ns and is assigned to product formation on S_0. The S_0 pathway appears to remain active at 317 nm, where a weak, but otherwise equivalent, feature grows in with a similar time constant of 58±23 ns. At 317 nm, the speed distribution is dominated at all time delays by fast moving CH_3 products formed on the T_1 surface, with most probable speeds around 1500 m s^{-1}. A similar, but far weaker feature at 320 nm extends slightly beyond v_{max} and likely arises from photolysis of residual vibrationally excited acetaldehyde due to incomplete cooling in the supersonic expansion. Products formed on T_1 do not appear promptly, but rather reach a maximum after tens of nanoseconds. At longer photolysis-probe delays, the magnitude of the T_1 component decays, although this is likely due to flyout of fast-moving photofragments from the small VUV probe laser focal volume. Products formed with velocities perpendicular to the probe propagation direction are particularly affected, leading to the ion images developing an artefactual anisotropy at longer delays. Finally, the broad, translationally fast components that decay with increasing delay are centered around 2400 m s^{-1} and extend far beyond v_{max}, indicating that a multi-photon process must be responsible. In contrast to the fast-moving products formed on T_1, however, the angular distributions remain isotropic, indicating that no flyout is occurring, despite the speeds being significantly greater. We will return to the origin of the multi-photon component in the discussion. Fitting to single-exponential decays yields time constants of 69±3 ns at 320 nm and 73±2 ns at 317 nm.

2. PHOFEX spectroscopy

PHOFEX action spectra of CH_3CHO were recorded by scanning the photolysis wavelength between 260–328 nm while monitoring the total two-color ion signals corresponding to CH_3 and HCO photolysis products. The spectra shown in Figure 8 were recorded using a photolysis-probe time delay of 40 ns, and have been corrected for a reproducible wavelength-dependent variation in the photolysis laser fluence. The PHOFEX spectra obtained probing CH_3 and HCO are identical across the

wavelength range and qualitatively reproduce the absorption band, including the diffuse structure present near the band maximum. A slight blue-shift of ~ 0.5 nm in the action spectrum is consistent with the low temperature of the molecular beam. Finer structure in the long wavelength region ($\lambda >$ 305 nm) reproduces that observed in analogous PHOFEX measurements reported by Cruse and Softley, who used 2+1 resonance-enhanced multiphoton ionization to state-selectively detect ground state CH_3 and HCO fragments.[29] The structure has been attributed to progressions in Franck-Condon active vibrational modes of the $S_1 \leftarrow S_0$ excitation, most probably combination bands of the CO stretch ν_4, CH_3 rock ν_{14}, and CH_3 torsion ν_{15} modes.[56,57] The expected yield of CH_3 and HCO, $Y_{IIa}(\lambda)$, can be calculated as the product of the absorption cross section and the photolysis quantum yield for channel IIa, both functions of the excitation wavelength:

$$Y_{IIa}(\lambda) = \sigma(\lambda)\Phi_{IIa}(\lambda)$$

$Y_{IIa}(\lambda)$ was calculated using the 295 K absorption cross section from the UV/VIS Spectral Atlas[58] and atmospheric pressure photolysis quantum yield data from Moortgat *et al.*[49] The predicted yield of channel IIa products, shown in Figure 8, is in excellent agreement with the PHOFEX spectra.

3. Picosecond time-resolved ion imaging

Time-resolved DC sliced velocity-map ion images of CH_3 products of the 266 nm photolysis of CH_3CHO were recorded using picosecond duration pulses and the same single-photon VUV ionization detection scheme. The time delay between the 266 nm and 118 nm pulses is defined as $\Delta t = t_{118} - t_{266}$. Consequently, $\Delta t > 0$ corresponds to the 266 nm pulse preceding the 118 nm ionization and two-color signals arise from 266 nm dissociation of neutral CH_3CHO, followed by subsequent VUV ionization of photoproducts. The measurements are complicated, however, by efficient ionization of the parent CH_3CHO at 118 nm. Reversing the time ordering of the pulses ($\Delta t < 0$), leads to significantly larger CH_3^+ signals due to photolysis of acetaldehyde cations by the 266 nm pulse. The rapid onset of CH_3^+ at negative delay times was used to characterize the 28 ps pulse duration, which

defines the measurement time resolution and serves as a convenient means to identify when photolysis and probe pulses were coincident.

Ion images of CH_3 products were recorded over a range of positive time delays spanning 0–1420 ps. The speed distributions shown in Figure 9 represent the increase in the signal at longer delays after subtraction of the earliest time delay data, which is dominated by a time-independent background signal caused by the high peak power of the picosecond pulses. The speed distributions are bimodal, comprising fast and slow components, and at the longest delay of 1420 ps is identical to that observed in the nanosecond experiments. The speed distributions were decomposed by fitting to Gaussian functions; centers and widths were determined from fitting the long-delay data and constrained in subsequent fits of data at shorter delays, allowing only the amplitudes to float. The change in the amplitudes of each component relative to the signal at the shortest delay is shown in Figure 10 alongside fits to a single exponential rise. The translationally fast component resulting from product formation on the T_1 surface is formed rapidly with a time constant of 240±50 ps while the translationally slow component, attributed to product formation on S_0, is also formed more slowly, with a time constant of 560±90 ps.

Discussion

1. Photolysis near the T_1 barrier: dissociation on S_0 and T_1

The height of the T_1 barrier leading to channel IIa products has been investigated by various groups using spectroscopic approaches[6,8,9] and from wavelength thresholds for product appearance.[27,29–32] Here, we use the barrier height of 31400±50 cm^{-1} determined in the ion imaging study of Amaral *et al.*, indicating a threshold wavelength of 318.5 nm for dissociation on the triplet surface.[31] This value is consistent with the 30953–31412 cm^{-1} range defined by Heazlewood *et al.*, who used laser-induced fluorescence to measure HCO radical product state distributions, conclusively demonstrating product formation on S_0 at photolysis wavelengths $\lambda > 318.35$ nm.[30] Excitation at 317 nm and 320

nm initially prepare acetaldehyde in S_1 with energies slightly above and below the apparent T_1 barrier.

The broad features with $v > v_{max}$ shown in Figure 7 that are common to speed distributions at both 317 nm and 320 nm appear promptly and decay exponentially with time constants of $\sim$70 ns. The time constants are broadly consistent with reported fluorescence lifetimes for the S_1 state in this wavelength range, suggesting that the time dependence of this component reflects the S_1 lifetime.[8,9,40,41] The spectrum of jet-cooled acetaldehyde shows rovibrational structure in this wavelength region and fluorescence lifetimes are strongly dependent on the excitation wavelength and often non-exponential.[9] The comparatively broad bandwidth (5–7 cm^{-1}) of the OPO inevitably spans multiple lines in the spectrum, which accounts for discrepancies between fluorescence lifetimes and the S_1 lifetime inferred from the time dependence of the transient dissociative ionization signal.

One plausible mechanism for formation of fast CH_3^+ is dissociative ionization of CH_3CHO in the S_1 state following absorption of a VUV photon. This process would be consistent with the absence of any fly-out anisotropy in the images, as the ions will have no significant velocity perpendicular to the molecular beam propagation direction. Sequential absorption of a UV and VUV photon provides a total energy of $\sim$14.4 eV relative to the ground state, which is above the CH_3^+ + HCO appearance energy of 14.08 eV but insufficient to account for the observed CH_3^+ speeds.[59–61] The CH_3^+ + HCO appearance energy coincides with excitation to the $\tilde{B}^2A'$ state of CH_3CHO^+, which is presumably dissociative, but inaccessible in a one-photon transition from the S_1 state of neutral CH_3CHO. Absorption of an additional photon of the relatively intense residual 355 nm (3.49 eV) radiation could drive the $\tilde{B}^2A'$–$\tilde{X}^2A'$ transition of the acetaldehyde cation, leading to dissociation and formation of fast CH_3^+.

Kable and co-workers have shown that the product state distribution for HCO formed on the S_0 surface is approximately statistical, while products formed on T_1 show evidence of impulsive dynamics.[30] In the vicinity of the T_1 barrier, both pathways were shown to be competitive, with dissociation on T_1 becoming increasingly dominant at shorter wavelengths. Ion imaging work by Amaral *et al.* shows CH_3 and HCO with E_T distributions that peak close to zero following photolysis at wavelengths that are too long to overcome the T_1 barrier, and are similar to those obtained at long delays following photolysis at 317 nm and 320 nm.[31] Phase Space Theory (PST)[62,63] and Separate Statistical Ensembles (SSE)[64] calculations have been performed using E_{AVL} = 2300 cm^{-1} and 2600 cm^{-1}, equivalent to excitation at 320 nm and 317 nm. The calculations model CH_3 and HCO as oblate and prolate symmetric tops, respectively, and used the rotational and vibrational constants reported by de Wit *et al.*[46] PST and SEE weight the product vibrational state distributions differently, based on the number of disappearing vibrational modes, although the distributions are almost indistinguishable.[64,65] The E_T distributions calculated using PST and SSE are shown in Figure 4 alongside the experimental data. The E_T distributions predicted by PST and SSE peak near zero and reproduce the observed slow component at both 317 and 320 nm reasonably well, consistent with unimolecular dissociation on the S_0 surface.

The appearance times for CH_3 formed on S_0 after photolysis at 317 nm and 320 nm are similar and in good agreement with variational transition state theory (VTST) calculations for various partially deuterated acetaldehyde isotopologues.[43,44] At energies corresponding to excitation at 323 nm and 330 nm, dissociation rates for the partially deuterated species were calculated to range between $k_D^{S_0}$ = 1–2×10^{-7} s^{-1}, indicating S_0 lifetimes of 50–100 ns. At 317 nm, the excitation energy is sufficient to overcome the T_1 barrier and dissociation on this surface is the dominant pathway to products. The S_0 pathway remains open, however, and accounts for around 15% of the products. Product formation on T_1 is significantly faster, with an appearance time constant of ~18 ns. The dissociation rate on the T_1 surface has been estimated using the standard RRKM expression

$$k(E) = \frac{N(E - E_0)}{h\rho(E)}$$

where $N(E - E_0)$ is the sum of states at the barrier and $\rho(E)$ is the T_1 density of states at the total energy E. Both E and E_0 are measured relative to the T_1 origin at 27240 cm^{-1}, giving a barrier height of 4160 cm^{-1}.[7,31] Harmonic vibrational frequencies (collected in Table 2) for the T_1 minimum and transition state were calculated at the CASSCF/def2-svp (18 electrons, 16 orbitals) level of theory using the MOLPRO 2012.1 quantum chemistry package.[66] Sums and densities of states were evaluated using the Stein-Rabinovitch algorithm as incorporated in the MULTIWELL package.[67] At 317 nm ($E = 4310$ cm^{-1}), the total energy is only 150 cm^{-1} above the barrier and the T_1 density of states is only around 6 per cm^{-1}. The RRKM dissociation rate is 1.6×10^{10} s^{-1}, which results in an exceptionally short T_1 lifetime of only 63 ps. Previous estimates of the T_1 density of states in this energy region have been significantly larger. Lee and Chen calculated 152 states per cm^{-1}, while inferring 518 states per cm^{-1} from fitting experimental fluorescence data.[9] These larger values of $\rho(E)$ extend the T_1 lifetime to a few nanoseconds, but are in general shorter than the observed CH_3 appearance time of $\sim$18 ns, suggesting that dissociation on T_1 is fast and $S_1 \rightarrow T_1$ intersystem crossing is rate-limiting. Direct $S_1 \rightarrow S_0$ internal conversion, $k_{IC}^{S_1 \rightarrow S_0}$, is likely to be slow relative to intersystem crossing, therefore the S_0 state is accessed by sequential intersystem crossing events $S_1 \rightarrow T_1 \rightarrow S_0$.[38] At 320 nm, the T_1 state is non-dissociative and can act as a temporary population reservoir. As phosphorescence is slow, the dominant loss processes are likely non-radiative, specifically intersystem crossing back to S_1 or to S_0. The small yield of products formed on S_0 following excitation in excess of the barrier indicates that the rate of $T_1 \rightarrow S_0$ intersystem crossing must be at least somewhat competitive with dissociation on the T_1 surface. Once the S_0 surface is reached, dissociation occurs statistically.

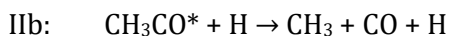## 2. Photolysis at λ ≤ 318 nm: Dissociation on the T_1 surface

Dissociation on the T_1 surface dominates beyond the threshold wavelength of 318.5 nm, and the available energy is partitioned primarily into translation. The E_T distributions evolve from being asymmetric with a sharp cut-off on the high-energy side near threshold, through symmetric near 292 nm, and becoming asymmetric again with a sharper drop on the low-energy edge at the shortest photolysis wavelengths. Figure 6 shows that both $\langle E_T \rangle$ and $\langle E_{INT} \rangle$ increase as the pump wavelength is decreased for products formed on T_1. This behavior is qualitatively consistent with the statistical adiabatic impulsive (SAI) model developed by Mordaunt et al.[68] in which energy is apportioned impulsively below the barrier and statistically above the barrier. The dynamics are predominantly impulsive near threshold and become increasingly statistical as the available energy is increased, which results in E_T distributions that shift to higher average values and broaden. Quasi-classical trajectories propagated on an *ab initio* T_1 surface by Thompson *et al*. qualitatively reproduce the evolution of the experimental E_T distributions as the available energy is increased.[37] HCO is predicted to remain vibrationally cold with additional excitation energy, while the low frequency ν_2 CH_3 umbrella mode becomes increasing populated. Fu *et al*. have performed trajectory surface hopping calculations to determine branching between the S_0 and T_1 pathways, finding that that majority of surface hops are due to intersystem crossing between $S_1 \rightarrow T_1$ and subsequently $T_1 \rightarrow S_0$.[38] The calculated E_T distributions for products formed on T_1 at 286 nm agree qualitatively with the experimental results, although the preferred method of dealing with violation of zero-point energy predicts a distribution that is narrower and peaks at lower E_T. A more significant discrepancy between the calculations and the experiments is the branching between product formation on S_0 and T_1. The calculations predict significant but monotonically decreasing yields of S_0 products at wavelengths that excite substantially above the T_1 barrier. At 286 nm, the S_0 branching is around 0.5. In contrast, the experiments show that the S_0 pathway quickly diminishes in importance with

increasing excitation energy. At 317 nm only ~15% of channel IIa products are formed on S_0, and contribute negligibly until S_0 photochemical pathways re-open at $\lambda < 292$ nm.

3. Photolysis at $\lambda \leq 292$ nm: Dissociation via S_1/S_0 conical intersection

The CH_3 product speed and total E_T distributions become bimodal at wavelengths shorter than 292 nm. Figure 5 shows that the new slow component appears weakly between 277–292 nm but grows more sharply relative to the T_1 component at $\lambda < 277$ nm, reaching around 40% at 265 nm. The total yield of channel IIa products, however, decreases steadily across this in this wavelength range as shown by the PHOFEX spectra in Figure 8. The bimodal E_T distribution at 266 nm is effectively identical to that measured previously by Shubert and Pratt, who also used VUV ionization at 119.46 nm (10.379 eV) to detect CH_3 and HCO.[42] The translational energy distributions extracted from CH_3 and HCO images were indistinguishable, indicating that internally excited HCO does not dissociate on the timescale of the measurement. At longer wavelengths in Region C, we also find good agreement with the E_T distributions obtained by Zhang *et al*. when state-selectively probing vibrational ground state products by 1+1 REMPI via the 0_0^0 band of the 4p–X̃ transition.[32] The slow component makes a much greater contribution when probing out-of-plane bend excited CH_3 products probed via the 2_1^1 band. Assuming that the VUV ionization is universal, this suggests that a) overall, CH_3 radicals are predominantly formed in their vibrational ground state, and b) the mechanism that leads to the slow component is more likely to result in out-of-plane bend excited CH_3 than the T_1 pathway. At 320 nm, products are formed on S_0 with a translational energy distribution that is well-described by SSE and PST statistical models. Figure 4 shows the predicted E_T distributions resulting from SSE and PST calculations for channel IIa with $E_{AVL} = 6020$ cm^{-1}, 7284 cm^{-1}, and 8645 cm^{-1}, corresponding to photolysis at 286 nm, 276 nm, and 266 nm. Overall, the agreement is poorer than at the longer wavelength as the experimental E_T distributions tend to peak further from zero than those predicted by the statistical theories. The short-wavelength slow component observed after photolysis in Region C cannot solely be described by a statistical distribution.

The appearance wavelength of the slow component is close to the threshold for the triple fragmentation channel III, which becomes energetically accessible at $\lambda < 294$ nm. Hobday *et al.* have suggested that the equivalent channel in formaldehyde (forming H + H + CO) accounts for up to 25% of products once the threshold wavelength is surpassed.[69] Stepwise fragmentation has been observed in studies of the photochemistry of acetone, wherein vibrationally hot CH_3CO radicals formed in a primary photolysis step undergo unimolecular decomposition to form CH_3 + CO.[70] Two-step PST calculations modeling triple fragmentation of acetaldehyde predict translationally slow products.[46] Triple fragmentation has been inferred at 248 nm, and could occur by secondary dissociation of internally excited methane, formyl, or acetyl initially formed via channels I, IIa and IIb:

I: $CH_4^* + CO \rightarrow CH_3 + H + CO$

IIa: $CH_3 + HCO^* \rightarrow CH_3 + H + CO$

IIb: $CH_3CO^* + H \rightarrow CH_3 + CO + H$

Highly internally excited CH_4 is associated with roaming, with FTIR measurements showing CH_4 products with an internal energy distribution that extended to the dissociation limit after excitation at 308 nm.[15] Barrierless decomposition of hot methane to form CH_3 + H would be anticipated to lead to a statistical disposal of the available energy beyond the threshold wavelength.[71,72] In contrast to channel I, barriers exist for secondary dissociation of formyl or acetyl radical products formed via channels IIa or IIb, which pushes the threshold to shorter wavelengths. The formyl and acetyl dissociation barriers are the subject of some uncertainty. For formyl, the barrier to dissociation has been determined primarily by measurements of the kinetics of the H + CO $\rightarrow$ HCO recombination reaction, with a value of 5780 ± 140 cm^{-1}.[73] High-level *ab initio* calculations have suggested that the experimental value is in error, and that a higher barrier of 6670 cm^{-1} is more appropriate.[74] Taken in combination with D_0 of 28950 cm^{-1} for channel IIa, this suggests a threshold wavelength in the

range 281–292 nm. Experimental estimates of the barrier to acetyl decomposition have been determined from photodissociation studies of acetone and acetyl chloride. North *et al.* observed that 30% of CH_3CO radicals formed from acetone dissociation at 248 nm decomposed and determined the barrier to be 6230±1100 cm^{-1}.[70] Tang *et al.* estimated a smaller value of 4970±170 cm^{-1} from similar experiments exploring acetyl chloride photodissociation.[75] Using D_0 = 30750 cm^{-1} for channel IIb, the threshold wavelength for secondary decomposition of acetyl likely falls in the range 271–281 nm.

While the thresholds for the triple fragmentation are broadly consistent with the onset of the slow component at shorter photolysis wavelengths, we think it unlikely to contribute significantly. Roaming is a relatively minor pathway to channel I products in Region C and the fraction of CH_4* with sufficient energy to dissociate will be smaller still.[18] Furthermore, two-step PST calculations modeling triple fragmentation predict E_T distributions that peak closer to zero than those for primary dissociation,[46] which appears to conflict with the single-step PST and SSE calculations. The application of PST to describe secondary dissociation of HCO* or CH_3CO* formed via channels IIa or IIb is questionable due to the presence of the barrier. A key assumption in PST is that the reaction coordinate along the potential energy surface does not influence the rate of combination, that is, dissociation is barrierless. The SAI model, which partitions the available energy into statistical and impulsive reservoirs has been used to model unimolecular dissociation of hot acetyl radicals and predicts a greater translational energy release.[68] Once again, only the fraction of acetyl radicals formed with energy greater than the dissociation barrier would dissociate and we see no evidence of any CH_3CO products. For HCO* products formed on T_1, $\langle E_{INT} \rangle$ is always significantly less than the height of the formyl barrier, as shown in Figure 6, suggesting only a small fraction would have sufficient energy to dissociate. More importantly, a stepwise process involving formation of channel IIa products, followed by unimolecular dissociation of HCO, would not affect the measured CH_3 speeds. Finally, we note that *all* secondary dissociation pathways should enhance the yield of methyl relative to that of formyl. Decomposition of hot CH_4 or CH_3CO via channels I and IIb would increase

the relative yield of CH_3, while decomposition of hot HCO yield would reduce its yield relative to CH_3. The PHOFEX spectra presented in Figure 8, however, show identical CH_3 and HCO yields at all excitation wavelengths, strongly suggesting that triple fragmentation is not occurring to any significant extent. Shubert and Pratt, also using single photon VUV ionization, have shown that the E_T distributions obtained from ion images of CH_3 and HCO products at 266 nm are consistent with there being no significant secondary dissociation of hot HCO, at least on the time scale of their measurements.[42]

Ohta and Baba originally suggested that a new non-radiative loss process may become available for higher levels of S_1 due to a second sharp decline in the fluorescence quantum yield at $\lambda < 280$ nm, in line with the onset of the translationally slow component in the CH_3 speed distributions observed in this work.[6] *Ab initio* calculations by Chen and Fang characterizing stationary points on the S_0, S_1 and T_1 surfaces suggest an explanation.[76] They identified a conical intersection between the S_1 and S_0 surfaces at extended C–C bond lengths that could serve as an efficient means of internal conversion prior to dissociation on the S_0 surface. Accessing the conical intersection, however, requires acetaldehyde to overcome a barrier on the S_1 surface of 5100 cm^{-1} relative to the origin. The S_1 barrier would imply a threshold wavelength of 287 nm, which is close to the onset observed experimentally. More recent calculations have predicted a range of barrier heights spanning energies of 6000–8000 cm^{-1} relative to the S_1 origin and correspond to threshold wavelengths between 265–279 nm.[19,38,76]

We propose that the translationally slow component of the CH_3 speed distribution in Region C results from accessing the S_1/S_0 conical intersection with subsequent dissociation on the S_0 surface. Indeed, it is unlikely to be coincidental that the total yield of molecular products (channel I) has the same wavelength dependence as CH_3 + HCO formed on S_0 shown in Figure 5. The dominance of the CH_4 + CO molecular channel at short wavelength arises as a result of dissociation via the S_1/S_0 conical intersection becoming competitive with intersystem crossing. This new pathway results in a non-

statistical distribution of the available energy, as evidenced by the marked deviation from SSE and PST predictions shown in Figure 4. The calculated conical intersection geometry has a C–C distance of 2.42 Å, which is significantly extended with respect to the equilibrium bond length of 1.51 Å for the S_0 state.[76] Consequently, the ensuing dynamics are likely dictated largely by long-range interactions between the nascent methyl and formyl radicals on the S_0 surface. A further bifurcation of the product flux between trajectories that sample the S_0 minimum and result in a statistical product state distribution and those which effectively skirt around the edge of the S_0 well, resulting in partitioning of a greater fraction of the E_{AVL} into relative translation, is also a possibility. From an experimental perspective, state-resolved detection of the CH_3 and HCO and complementary trajectory calculations on accurate potential energy surfaces would shed further light on the details of the mechanism.

The bimodal CH_3 speed distribution observed using the nanosecond laser systems at 266 nm is also observed at picosecond delays, as shown in Figure 9. The fast and slow components, attributed to dissociation on T_1 and S_0 via the S_1/S_0 conical intersection, respectively, are formed with different single-exponential rise time constants. The major T_1 component is formed quickly with a rate $(4.2 \pm 0.8) \times 10^9$ s^{-1}, while the smaller translationally slow component is also formed more slowly with a rate of $(1.8 \pm 0.3) \times 10^9$ s^{-1}. For products formed on T_1, the observed rate could be due to either the rate of $S_1 \rightarrow T_1$ intersystem crossing, $k_{ISC}^{S_1 \rightarrow T_1}$, or the rate of dissociation to products once on the T_1 surface, $k_D^{T_1}$. The latter can again be estimated using RRKM theory. Excitation at 266 nm prepares acetaldehyde in S_1 with an energy 6195 cm^{-1} above the T_1 barrier. The RRKM calculations predict $k_D^{T_1} = 7.6 \times 10^{11}$ s^{-1} and a lifetime on the T_1 surface of only 1.3 ps. This is two orders of magnitude faster than the observed CH_3 formation rate, suggesting that dissociation on T_1 is comparatively prompt and not rate limiting. Consequently, we attribute the observed formation rate of the translationally fast component to the rate of $S_1 \rightarrow T_1$ intersystem crossing.

Previously, Abou-Zied and McDonald used picosecond time-resolved REMPI detection to measure single-exponential rise-times of 667±43 ps and 662±34 ps for CH_3CO and HCO products, respectively, following photolysis of acetaldehyde at 266 nm. The time-dependent yield of HCO was measured using 2+1 REMPI via the 3p $^2\Pi$ state near 400 nm. The appearance times are significantly longer than that determined in this work for the predominant T_1 pathway but in reasonable agreement with the rise time of 560±90 ps measured for the smaller S_0 component. The REMPI measurements may not probe HCO product quantum states that are preferentially populated by dissociation on the T_1 surface, biasing the detection in favor of products formed on S_0. Abou-Zied and McDonald noted that they were unable to detect any time-dependent signal at photolysis wavelengths in the range 280–315 nm, which is consistent with this hypothesis; the S_0 pathway is a minor (<15 %) contributor in the 280–292 nm range, and is not observed at all at $\lambda > 292$ nm. The observation of acetyl products at all is also somewhat at odds with our measurements, although the detection sensitivity of single photon VUV ionization could be significantly poorer than the unspecified REMPI scheme used to detect CH_3CO in the earlier work. We note that other groups have argued that acetyl products are not formed at the nearby photolysis wavelength of 248 nm.[47,48] The barrier on the T_1 surface for formation of channel IIb products is ~4000 cm^{-1} higher than for channel IIa,[76] while unimolecular decomposition rates on S_0 also strongly favor channel IIa.[44]

For the short-wavelength S_0 pathway, there are two steps that are likely rate limiting for product formation: the rate of passage over the S_1 barrier, $k_{TS}^{S_1}$, leading to the conical intersection or the rate of dissociation to products once on the S_0 surface, $k_D^{S_0}$. We consider first the possibility that $k_{TS}^{S_1}$ is rate limiting by comparison with RRKM calculations using harmonic frequencies calculated at the CASSCF/def2-svp level as before. The RRKM rate is highly sensitive to the barrier height. Using the observed onset $\lambda = 292$ nm results in a rate of, $k_{TS}^{S_1} = 6.6 \times 10^{11}$ s^{-1} and a lifetime of only 1.5 ps. A barrier of 6520 cm^{-1}, in the middle of the range predicted by theory, however, results in $k_{TS}^{S_1} =$

1.7×10^7 s^{-1}, corresponding to a lifetime of 150 ps which is again faster than the observed rise time. However, if passage over the S_1 transition state is fast and the observed formation rate instead reflects $k_D^{S_0}$, one would expect a ratio of T_1 to S_0 products that was strongly in favor of the latter. That the ratio of the formation rates is close to the observed branching ratios, suggests that they share S_1 as a common precursor state. Assuming passage over the S_1 TS to be rate limiting, the lifetime of the S_1 state is estimated to be ~170 ps after excitation at 266 nm, consistent with the sub-ns fluorescence lifetime observed at wavelengths shorter than 280 nm.[6] The branching could be modified to some extent by other dissociation channels once on S_0, such as the formation of molecular products. Dissociation over the conventional S_0 transition state to form $CH_4 + CO$ is calculated to have an RRKM rate 2.5×10^8 s^{-1} (4 ns), approximately an order of magnitude slower than the CH_3 appearance rate. The time scale for dissociation via roaming has not been determined experimentally, but state-resolved measurements probing CO products with picosecond time resolution are likely to be insightful.

Conclusions

Ion imaging and PHOFEX action spectroscopy with single-photon VUV detection of products have been used to explore the photochemistry of acetaldehyde across a broad wavelength range (265–328 nm) spanning the first absorption band. The radical channel IIa, leading to CH_3 and HCO products, can be categorized into three distinct photolysis wavelength regions. Region A ($\lambda > 318$ nm) corresponds to excitation energies below the T_1 barrier and CH_3 products are formed with translational energy distributions that are consistent with statistical model predictions for unimolecular dissociation on the S_0 surface. Dissociation is slow; at 320 nm, products are formed with a single-exponential rise time of 66±9 ns, consistent with predictions of VTST. In Region B ($\lambda \leq$ 318 nm) dissociation over the barrier on the T_1 surface becomes energetically accessible and product formation on S_0 effectively ceases. Near the T_1 threshold, radical products are formed with a narrow

distribution of recoil speeds that peaks close to the maximum allowed by energy conservation, v_{max}. The distributions broaden and deviate increasingly from v_{max} as the photolysis wavelength is decreased, consistent with increased partitioning of the available energy into internal degrees of freedom of the radicals as predicted by mixed statistical/impulsive models. In Region C ($\lambda < 292$ nm) a new pathway opens that produces translationally slow, but non-statistical, CH_3 radicals. This new pathway becomes increasingly competitive with dissociation on T_1 at shorter wavelengths. PHOFEX spectra of acetaldehyde probing CH_3 and HCO products between 260–328 nm are identical, an observation incompatible with the three-body fragmentation channel III, which has a threshold wavelength near the onset of the new translationally slow component. It is proposed that the new component results from dissociation on S_0 after internal conversion via a conical intersection between the S_1 and S_0 surface that can be accessed over a barrier on the S_1 surface at extended C–C bond lengths. Time-resolved ion imaging measurements using picosecond duration pulses at a photolysis wavelength of 266 nm show that products are formed via the T_1 and S_0 pathways with different, but competitive, rates of 4.2×10^9 s^{-1} and 1.8×10^9 s^{-1}, respectively. The former is attributed to the rate for $S_1 \rightarrow T_1$ intersystem crossing and the latter primarily to the rate of passage over the S_1 barrier, prior to accessing the S_1/S_0 conical intersection.

Acknowledgements

References

1 J. B. Burkholder, S. P. Sander, J. Abbatt, J. R. Barker, R. E. Huie, C. E. Kolb, M. J. Kurylo, V. L. Orkin, D. M. Wilmouth, and P. H. Wine "Chemical Kinetics and Photochemical Data for Use in Atmospheric Studies, Evaluation No. 18," JPL Publication 15-10, Jet Propulsion Laboratory, Pasadena, 2015 http://jpldataeval.jpl.nasa.gov, .

2 H. Liu, E. C. Lim, R. H. Judge and D. C. Moule, J. Chem. Phys., 1995, **102**, 4315–4320.

3 M. Noble, E. C. Apel and E. K. C. Lee, J. Chem. Phys., 1983, **78**, 2219–2226.

4 M. Noble and E. K. C. Lee, J. Chem. Phys., 1984, **80**, 134–139.

5 M. Noble and E. K. C. Lee, J. Chem. Phys., 1984, **81**, 1632–1642.

6 N. Ohta and H. Baba, J. Phys. Chem., 1986, **90**, 2654–2661.

7 H. Liu, E. C. Lim, C. Muñoz-Caro, A. Niño, R. H. Judge and D. C. Moule, J. Chem. Phys., 1996, **105**, 2547–2552.

8 T. Gejo, H. Bitto and J. R. Huber, Chem. Phys. Lett., 1996, **261**, 443–449.

9 S.-H. Lee and I.-C. Chen, Chem. Phys., 1997, **220**, 175–189.

10 C.-L. Huang, V. Chien, I.-C. Chen, C.-K. Ni and A. H. Kung, J. Chem. Phys., 2000, **112**, 1797–1803.

11 B. Ruscic, .

12 B. F. Gherman, R. A. Friesner, T.-H. Wong, Z. Min and R. Bersohn, J. Chem. Phys., 2001, **114**, 6128–6133.

13 Y. Kurosaki and K. Yokoyama, J. Phys. Chem. A, 2002, **106**, 11415–11421.

14 Y. Kurosaki, Chem. Phys. Lett., 2006, **421**, 549–553.

15 P. L. Houston and S. H. Kable, Proc. Natl. Acad. Sci., 2006, **103**, 16079–16082.

16 L. Rubio-Lago, G. A. Amaral, A. Arregui, J. G. Izquierdo, F. Wang, D. Zaouris, T. N. Kitsopoulos and L. Bañares, Phys. Chem. Chem. Phys., 2007, **9**, 6123–6127.

17 B. R. Heazlewood, M. J. T. Jordan, S. H. Kable, T. M. Selby, D. L. Osborn, B. C. Shepler, B. J. Braams and J. M. Bowman, Proc. Natl. Acad. Sci., 2008, **105**, 12719–12724.

18 L. Rubio-Lago, G. A. Amaral, A. Arregui, J. González-Vázquez and L. Bañares, Phys. Chem. Chem. Phys., 2012, **14**, 6067–6078.

19 D. Townsend, S. A. Lahankar, S. K. Lee, S. D. Chambreau, A. G. Suits, X. Zhang, J. Rheinecker, L. B. Harding and J. M. Bowman, Science, 2004, **306**, 1158–1161.

20 A. G. Suits, Acc. Chem. Res., 2008, **41**, 873–881.

21 J. M. Bowman and B. C. Shepler, Annu. Rev. Phys. Chem., 2011, **62**, 531–553.

22 B. C. Shepler, B. J. Braams and J. M. Bowman, J. Phys. Chem. A, 2007, **111**, 8282–8285.

23 B. C. Shepler, B. J. Braams and J. M. Bowman, J. Phys. Chem. A, 2008, **112**, 9344–9351.

24 K. L. K. Lee, M. S. Quinn, A. T. Maccarone, K. Nauta, P. L. Houston, S. A. Reid, M. J. T. Jordan and S. H. Kable, Chem. Sci., 2014, **5**, 4633–4638.

25 A. Horowitz and J. G. Calvert, J. Phys. Chem., 1982, **86**, 3105–3114.

26 A. Horowitz, C. J. Kershner and J. G. Calvert, J. Phys. Chem., 1982, **86**, 3094–3105.

27 T. Kono, M. Takayanagi, T. Nishiya and I. Hanazaki, Chem. Phys. Lett., 1993, **201**, 166–170.

28 S.-H. Lee and I.-C. Chen, J. Chem. Phys., 1996, **105**, 4597–4604.

29 H. A. Cruse and T. P. Softley, J. Chem. Phys., 2005, **122**, 124303.

30 B. R. Heazlewood, S. J. Rowling, A. T. Maccarone, M. J. T. Jordan and S. H. Kable, J. Chem. Phys., 2009, **130**, 054310.

31 G. A. Amaral, A. Arregui, L. Rubio-Lago, J. D. Rodríguez and L. Bañares, J. Chem. Phys., 2010, **133**, 064303.

32 Z. Zhang, Z. Chen, C. Zhang, Y. Jin, Q. Zhang, Y. Chen, C. Huang and X. Yang, Chin. J. Chem. Phys., 2014, **27**, 249–255.

33 A. C. Terentis, M. Stone and S. H. Kable, J. Phys. Chem., 1994, **98**, 10802–10808.

34 T. Gejo, M. Takayanagi, T. Kono and I. Hanazaki, Chem. Phys. Lett., 1994, **218**, 343–348.

35 J. S. Yadav and J. D. Goddard, J. Chem. Phys., 1986, **84**, 2682–2690.

36 Y. Kurosaki and K. Yokoyama, Chem. Phys. Lett., 2003, **371**, 568–575.

37 K. C. Thompson, D. L. Crittenden, S. H. Kable and M. J. T. Jordan, J. Chem. Phys., 2006, **124**, 044302.

38 B. Fu, Y. Han and J. M. Bowman, Faraday Discuss., 2012, **157**, 27–39.

39 O. K. Abou-Zied and J. D. McDonald, J. Chem. Phys., 1998, **109**, 1293–1301.

40 G.-H. Leu, C.-L. Huang, S.-H. Lee, Y.-C. Lee and I.-C. Chen, J. Chem. Phys., 1998, **109**, 9340–9350.

41 C.-L. Huang, V. Chien, C.-K. Ni, A. H. Kung and I.-C. Chen, J. Phys. Chem. A, 2000, **104**, 10362–10367.

42 V. A. Shubert and S. T. Pratt, J. Phys. Chem. A, 2010, **114**, 11238–11243.

43 B. R. Heazlewood, A. T. Maccarone, D. U. Andrews, D. L. Osborn, L. B. Harding, S. J. Klippenstein, M. J. T. Jordan and S. H. Kable, Nat. Chem., 2011, **3**, 443–448.

44 D. U. Andrews, B. R. Heazlewood, A. T. Maccarone, T. Conroy, R. J. Payne, M. J. T. Jordan and S. H. Kable, Science, 2012, **337**, 1203–1206.

45 A. E. Clubb, M. J. T. Jordan, S. H. Kable and D. L. Osborn, J. Phys. Chem. Lett., 2012, 3522–3526.

46 G. de Wit, B. R. Heazlewood, M. S. Quinn, A. T. Maccarone, K. Nauta, S. A. Reid, M. J. T. Jordan and S. H. Kable, Faraday Discuss., 2012, **157**, 227–241.

47 P. Morajkar, A. Bossolasco, C. Schoemaecker and C. Fittschen, J. Chem. Phys., 2014, **140**, 214308.

48 K.-C. Hung, P.-Y. Tsai, H.-K. Li and K.-C. Lin, J. Chem. Phys., 2014, **140**, 064313.

49 G. K. Moortgat, H. Meyrahn and P. Warneck, ChemPhysChem, 2010, **11**, 3896–3908.

50 B. W. Toulson, J. P. Alaniz, J. G. Hill and C. Murray, Phys. Chem. Chem. Phys., 2016, **18**, 11091–11103.

51 D. Townsend, M. P. Minitti and A. G. Suits, Rev. Sci. Instrum., 2003, **74**, 2530–2539.

52 A. H. Kung, J. F. Young and S. E. Harris, Appl. Phys. Lett., 1973, **22**, 301–302.

53 C. A. Taatjes, D. L. Osborn, T. M. Selby, G. Meloni, H. Fan and S. T. Pratt, J. Phys. Chem. A, 2008, **112**, 9336–9343.

54 B. Gans, L. A. V. Mendes, S. Boyé-Péronne, S. Douin, G. Garcia, H. Soldi-Lose, B. K. C. de Miranda, C. Alcaraz, N. Carrasco, P. Pernot and D. Gauyacq, J. Phys. Chem. A, 2010, **114**, 3237–3246.

55 F. Aguirre and S. T. Pratt, J. Chem. Phys., 2005, **122**, 234303.

56 M. Baba, I. Hanazaki and U. Nagashima, J. Chem. Phys., 1985, **82**, 3938–3947.

57 T. Kono, M. Takayanagi and I. Hanazaki, J. Phys. Chem., 1993, **97**, 12793–12797.

58 H. Keller-Rudek, G. K. Moortgat, R. Sander and R. Sörensen, Earth Syst. Sci. Data, 2013, **5**, 365–373.

59 H. W. Jochims, W. Lohr and H. Baumgärtel, Chem. Phys. Lett., 1978, **54**, 594–596.

60 R. Bombach, J.-P. Stadelmann and J. Vogt, Chem. Phys., 1981, **60**, 293–299.

61 K. Johnson, I. Powis and C. J. Danby, Chem. Phys., 1982, **70**, 329–343.

62 P. Pechukas and J. C. Light, J. Chem. Phys., 1965, **42**, 3281–3291.

63 P. Pechukas, J. C. Light and C. Rankin, J. Chem. Phys., 1966, **44**, 794–805.

64 C. Wittig, I. Nadler, H. Reisler, M. Noble, J. Catanzarite and G. Radhakrishnan, J. Chem. Phys., 1985, **83**, 5581–5588.

65 W. H. Green, C. B. Moore and W. F. Polik, Annu. Rev. Phys. Chem., 1992, **43**, 591–626.

66 H.-J. Werner, P. J. Knowles, G. Knizia, F. R. Manby and M. Schütz, Wiley Interdiscip. Rev. Comput. Mol. Sci., 2012, **2**, 242–253.

67 Barker, J. R. et al., MultiWell-2016 Software Suite; J. R. Barker, University of Michigan, Ann Arbor, Michigan, USA, 2016; http://clasp-research.engin.umich.edu/multiwell/, 2016.

68 D. H. Mordaunt, D. L. Osborn and D. M. Neumark, J. Chem. Phys., 1998, **108**, 2448–2457.

69 N. Hobday, M. S. Quinn, K. Nauta, D. U. Andrews, M. J. T. Jordan and S. H. Kable, J. Phys. Chem. A, 2013, **117**, 12091–12103.

70 S. W. North, D. A. Blank, J. D. Gezelter, C. A. Longfellow and Y. T. Lee, J. Chem. Phys., 1995, **102**, 4447–4460.

71 A. Dutta and C. D. Sherrill, J. Chem. Phys., 2003, **118**, 1610–1619.

72 L. B. Harding, S. J. Klippenstein and A. W. Jasper, Phys. Chem. Chem. Phys., 2007, **9**, 4055–4070.

73 H. Y. Wang, J. A. Eyre and L. M. Dorfman, J. Chem. Phys., 1973, **59**, 5199–5200.

74 P. S. Peters, D. Duflot, L. Wiesenfeld and C. Toubin, J. Chem. Phys., 2013, **139**, 164310.

75 X. Tang, B. J. Ratliff, B. L. FitzPatrick and L. J. Butler, J. Phys. Chem. B, 2008, **112**, 16050–16058.

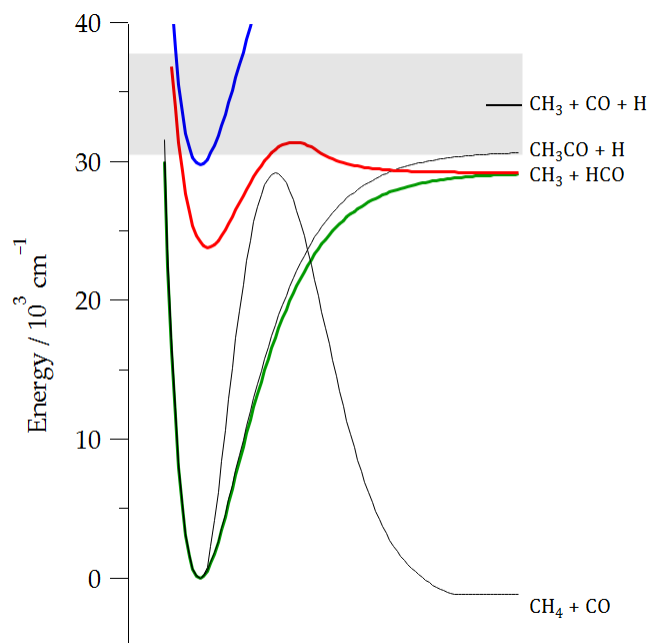76 S. Chen and W.-H. Fang, J. Chem. Phys., 2009, **131**, 054306.

Figures

Figure 1. Schematic potential energy surfaces and dissociation channels for acetaldehyde. The shaded gray area represents the range of photolysis wavelengths used.
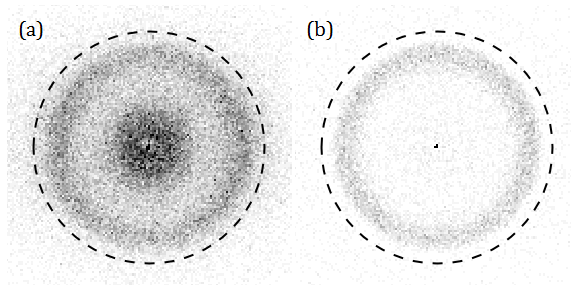
Figure 2 DC slice ion images of CH_3 products from the photolysis of CH_3CHO at 308 nm. Image (a) was recorded with clusters were present in the expansion, while image (b) was recorded under cluster-free conditions. The dashed circle indicates the maximum CH_3 speed, determined by energy conservation.
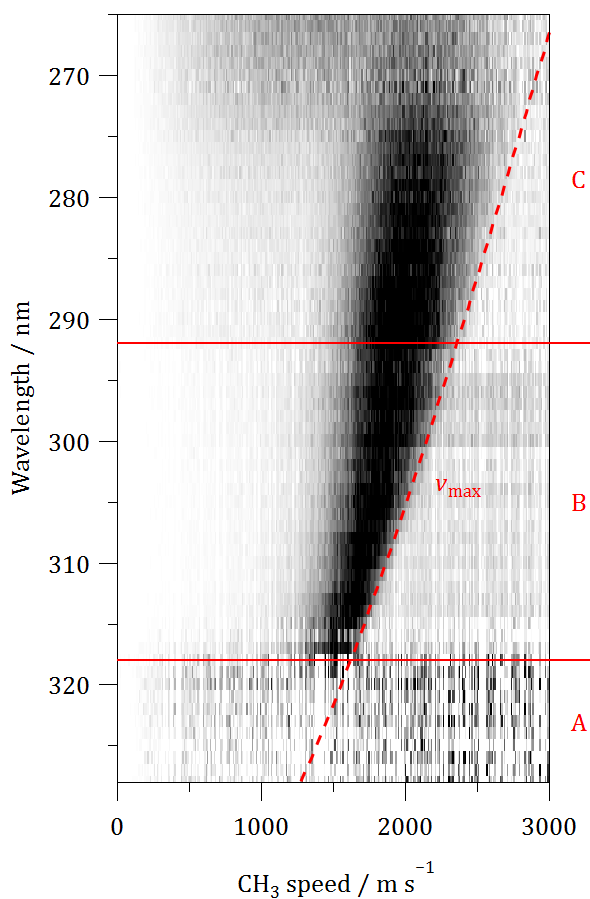
Figure 3. Intensity plot showing normalized CH_3 speed distributions from photolysis of CH_3CHO over the wavelength range 265–328 nm. The curved dashed line indicates the maximum CH_3 speed, v_{max}, determined by energy conservation. Region A corresponds to excitation to S_1 at energies below the T_1 barrier and results in no significant CH_3 production at the photolysis-probe delay of 40 ns; Region B is dominated by fast-moving CH_3 formed by dissociation on the T_1 surface; and Region C sees the appearance of a new translationally slow component that is attributed to non-statistical dissociation on S_0 as described in the text.
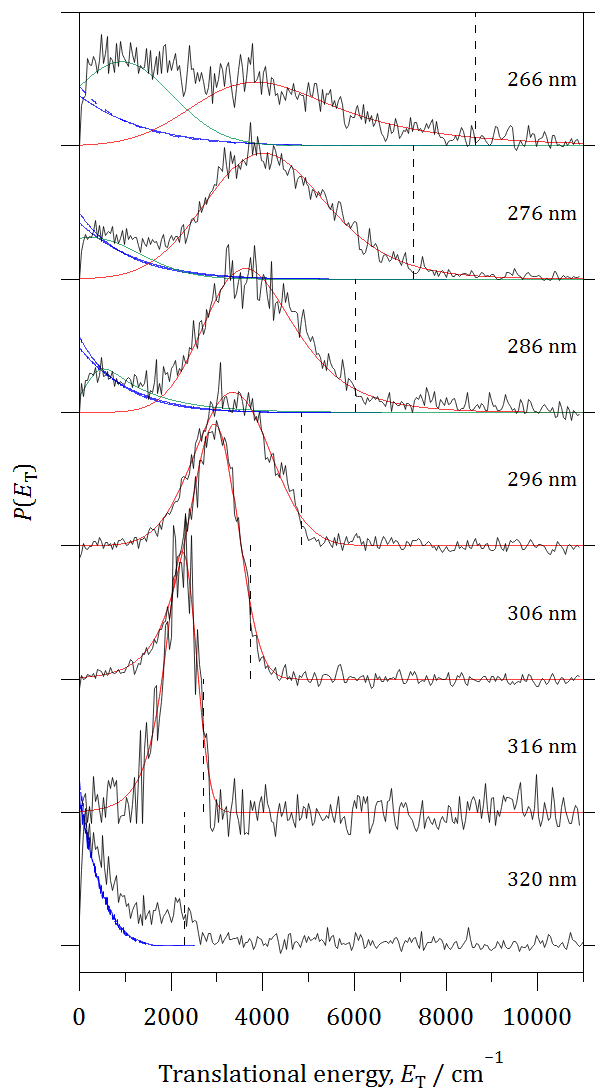
Figure 4. Normalized product translational energy distributions following photolysis of CH_3CHO at the indicted wavelengths spanning 266–320 nm. The 320 nm data were recorded with a photolysis-probe delay of 210 ns, while all other wavelengths used a delay of 40 ns. Dashed vertical lines indicate the energetic limits at each photolysis wavelength. The green and red curves are fits to the E_T distributions attributed to products formed on the S_0 and T_1 surfaces, respectively. Blue curves are the predictions for unimolecular dissociation from phase space theory (solid) and separate statistical ensembles (dashed) calculations.
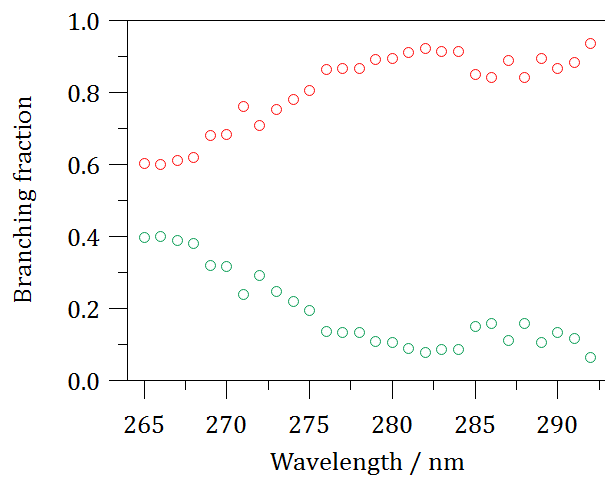
Figure 5. Branching between T_1 (red) and S_0 via the S_1/S_0 conical intersection (green) pathways derived from $P(E_T)$ distributions in Region C.
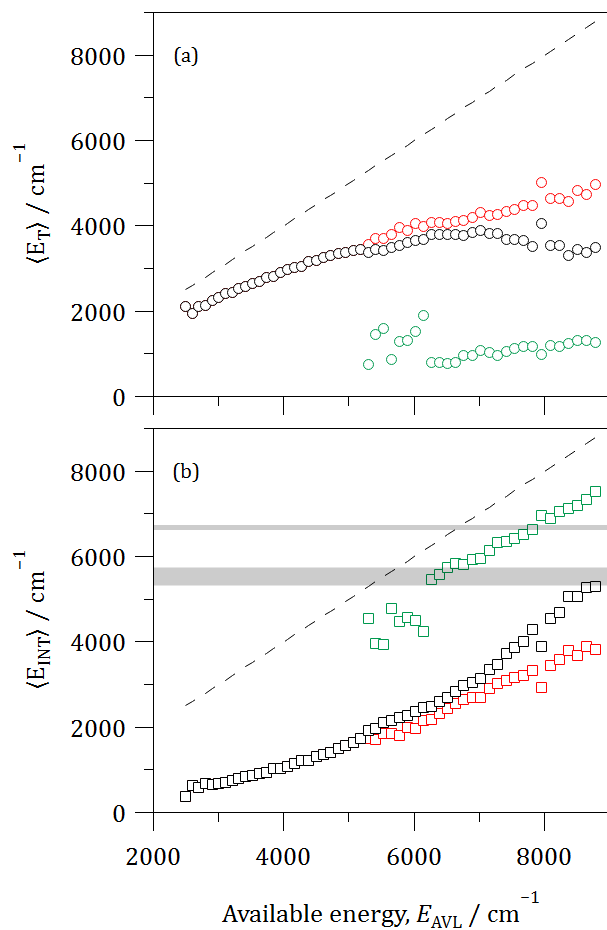
Figure 6. (a) Average translational as a function of available energy for products formed on T_1 (red), S_0 (green), and overall (black). (b) Average radical internal energy as a function of available energy. Shaded areas indicate experimental or theoretical barriers for dissociation of HCO as discussed in the text.
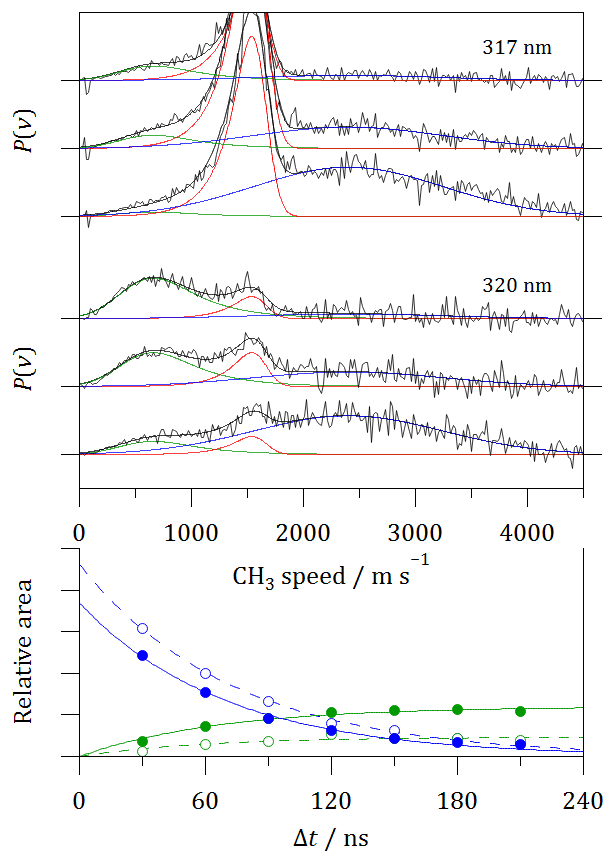
Figure 7. Time-resolved CH$_3$ speed distributions from the photolysis of acetaldehyde at 317 nm and 320 nm. Data shown are for photolysis probe delays of 210 ns, 90 ns and 30 ns (top to bottom). The speed distributions are decomposed into components corresponding to product formation on S$_0$ via internal conversion (green), T$_1$ (red) and transient dissociative ionization of S$_1$ (blue). The lower panel shows the time dependence of the S$_1$ and S$_0$ components at 317 nm (open circles) and 320 nm (filled circles).
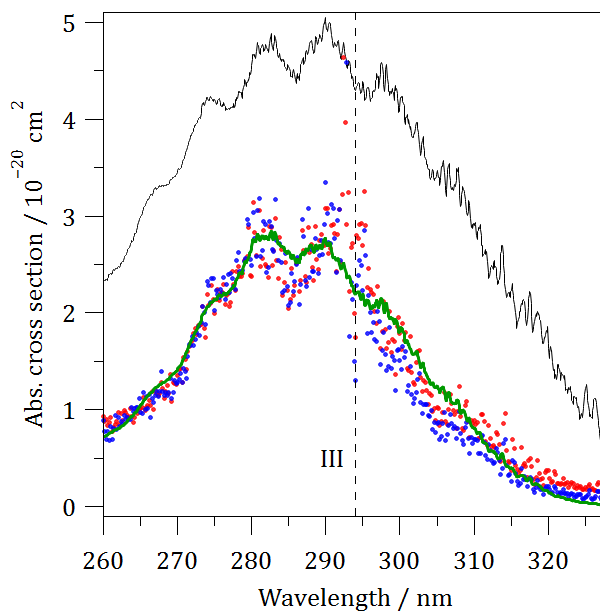
Figure 8. Acetaldehyde PHOFEX action spectra recorded probing CH_3 (blue) and HCO (red) products by single-photon VUV ionization alongside the conventional absorption spectrum (black) at 294 K. The PHOFEX spectra have been scaled to match the predicted product yield (green) calculated as the product of the wavelength-dependent absorption cross section and photolysis quantum yield for the CH_3 + HCO channel.
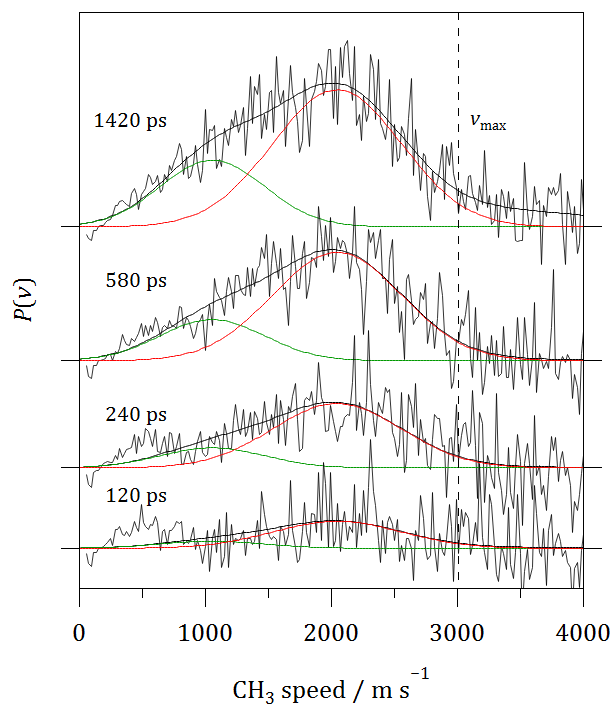
Figure 9. Time evolution of the CH_3 speed distributions following photolysis of CH_3CHO at 266 nm using 28 ps pulses. The green and red curves are fits to the speed distributions attributed to products formed on the S_0 and T_1 surfaces, respectively.
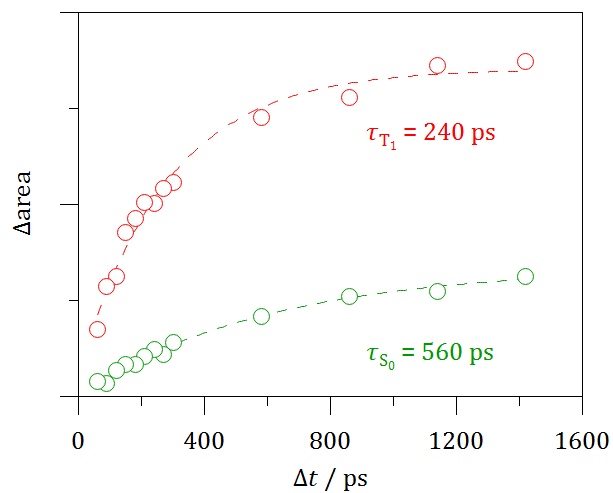
Figure 10. Time dependence of slow (green) and fast (red) components of the CH_3 speed distributions obtained at 266 nm. The data have been fit to a single exponential rise to obtain time constants for product formation.

Tables

Table 1. Product formation and transient dissociative ionization time constants.

λ / nm	320	317	266
		τ / ns	
S_0 formation	66±9	58±23	0.56±0.09
T_1 formation	54±5	18±2	0.24±0.05
S_1 decay	69±3	73±2	–

Table 2. Harmonic frequencies for acetaldehyde calculated at the CASSCF/def2-svp level of theory.

	T_1 min	S_1 min	T_1 TS	S_1 TS
ν_1	3259	3293	3394	3397
ν_2	3028	3229	3304	3387
ν_3	2985	2989	3176	3299
ν_4	2923	2923	3073	3038
ν_5	1544	1570	1555	1539
ν_6	1510	1536	1519	1529
ν_7	1443	1481	1483	1474
ν_8	1391	1368	1128	1206
ν_9	1195	1182	1068	1050
ν_{10}	1125	1132	825	724
ν_{11}	1072	1074	714	668
ν_{12}	968	964	650	654
ν_{13}	666	654	314	323
ν_{14}	414	399	129	47
ν_{15}	208	206	679i	837i